Terahertz generation in nitrides due to transit-time resonance assisted by optical phonon emission

2008 J. Phys.: Condens. Matter 20 384209

(http://iopscience.iop.org/0953-8984/20/38/384209)

J. Phys.: Condens. Matter **20** (2008) 384209 (12pp) doi:10.1088/0953-8984/20/38/384209

Terahertz generation in nitrides due to transit-time resonance assisted by optical phonon emission

E Starikov[1], P Shiktorov[1], V Gružinskis[1], L Varani[2], C Palermo[2], J-F Millithaler[3] and L Reggiani[3]

[1] Semiconductor Physics Institute, A Goštauto 11, 01108 Vilnius, Lithuania
[2] Institut d'Électronique du Sud (CNRS UMR 5214), Université Montpellier 2, Place Eugène Bataillon, 34095 Montpellier Cedex 5, France
[3] Dipartimento di Ingegneria dell'Innovazione and CNISM, Università del Salento, Via Arnesano s/n, I-73100 Lecce, Italy

E-mail: jane@pav.pfi.lt (J-F Millithaler)

Received 25 March 2008, in final form 6 May 2008
Published 21 August 2008
Online at stacks.iop.org/JPhysCM/20/384209

Abstract
The conditions for THz radiation generation caused by electron transit-time resonance in momentum and real spaces under optical phonon emission are analyzed for nitride-based materials and their structures. It is shown that such a mechanism provides a unique possibility to realize sub-THz and THz radiation generation at the border between the electro-optical and electronic techniques by using two alternative approaches: (i) amplification of transverse electromagnetic waves in 3D bulk materials and 2D quantum wells, and (ii) longitudinal current–field instabilities in sub-micron and micron n^+nn^+ diodes. Estimations of frequency regions, output power and efficiency of the generation demonstrate that nitrides are promising materials for THz radiation generation.

1. Introduction

It is well known that THz represents a frequency at the border between regions exploiting two different ways for achieving electromagnetic radiation generation, namely: from below, ultra-high frequency electronics and, from above, far-infrared photonics. In the former case, the generation is due to *longitudinal electrical waves* instabilities (as in Gunn-devices, IMPATT-diodes, etc) which exploit static negative differential conductivity (NDC) of the N- or S-type, which starts from zero frequency and ends at some cutoff frequency. In the latter case, generation is due to amplification of *transverse electromagnetic waves* (as in quantum cascade lasers, hot-carrier p-Ge lasers, etc) which exploit population inversion between some energy states. Here, the amplification/generation process is usually described in terms of the amplification coefficients (or dynamical NDC) which take place in restricted regions near certain resonant frequencies. In each of these ways, the generation efficiency decreases significantly when trying to extend into the THz region. Therefore, identifying the physical mechanisms which lead to THz generation making use of both ways is a mandatory issue. The aim of this work is to show that the electron transit-time resonance in momentum and real spaces under low-temperature optical phonon emission is an effective mechanism to address such an issue. To support this conjecture we shall review recent theoretical predictions on THz generation due to transit-time resonance assisted by optical phonon emission in nitride-based three-dimensional (3D) bulk materials, two-dimensional (2D) quantum heterostructures, and sub-micron or micron n^+nn^+ diodes.

The content of the paper is organized as follows. Section 2 briefly reviews the concept and properties of the transit-time resonance. Section 3 considers the amplification and generation of transverse electromagnetic waves in bulk semiconductors and 2D structures. Section 4 is devoted to current instabilities in n^+nn^+ structures induced by excitation of longitudinal electric waves. Major conclusions are presented in section 5.

2. Transit-time resonance: concept and properties

At sufficiently low lattice temperatures, when the mechanism of absorption of optical phonons with energy $\hbar\omega_0$ by free

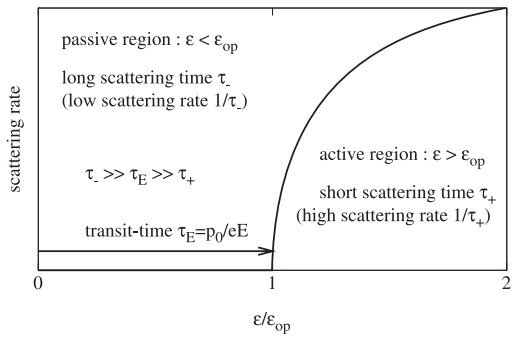

Figure 1. Schematic representation of the momentum space subdivision into a passive and an active region with respect to optical phonon energy.

carriers is practically absent so that $T \ll \hbar\omega_0/k_B$ (with k_B being the Boltzmann constant), the threshold onset for optical phonon emission subdivides the momentum space, **p**, into two regions, the so called passive and active ones. In the *passive* region, where the carrier energy $\varepsilon(\mathbf{p})$ is less than $\hbar\omega_0$, optical phonon emission is absent and carriers undergo only weak quasi-elastic scatterings caused by deformation and piezoelectric acoustic phonons, as well as impurity ions with combined characteristic momentum relaxation time τ_-. In the *active* region, where $\varepsilon(\mathbf{p}) > \hbar\omega_0$ spontaneous emission of optical phonons with the characteristic scattering time

$$\tau_+ \ll \tau_- \tag{1}$$

is switched on. Such a situation is schematically represented in figure 1.

With a dc electric field E being applied to the semiconductor structure, in the passive region a carrier can move (quasi-)ballistically up to the optical phonon boundary if τ_- satisfies the condition:

$$\tau_E \ll \tau_- \tag{2}$$

where $\tau_E = p_0/eE$ is the transit-time necessary for a carrier starting from the origin of momentum space to reach its boundary at $p_0 = \sqrt{2m_0m^*\hbar\omega_0}$. Here, within a simple spherical and parabolic band, p_0 is the radius of the optical phonon sphere in momentum space, m_0 and m^* the free and effective electron mass, respectively.

By supposing that the condition (2) is fulfilled, the electron penetration into the active region can display the following scenario. If the penetration is sufficiently small, that is:

$$\delta\varepsilon \ll \hbar\omega_0 \tag{3}$$

$\delta\varepsilon$ being the penetration energy, a carrier quickly emits an optical phonon and comes back near the center of the passive region. In terms of the characteristic times, this condition is usually formulated as:

$$\tau_+ \ll \tau_E. \tag{4}$$

As a consequence, when the conditions (2) and (4) are satisfied, carrier motion in momentum space takes the well-known cyclic character. Starting from the center of the passive region it moves quasi-ballistically during time τ_E, then it quickly emits an optical phonon and returns back to the center of the passive region, thus starting the next cycle. In real space, such a periodic process in momentum space corresponds to a generally forward motion consisting of free accelerations in the field direction followed by stops occurring when the carrier, after emitting an optical phonon, takes a near to zero velocity. The spatial period of such an acceleration-stop motion is determined by the real-space path which is necessary for a carrier to achieve the optical phonon energy $\hbar\omega_0$ due to the acceleration in the dc electric field:

$$l_0 = \frac{eE}{m_0m^*}\frac{\tau_E^2}{2} = \frac{\hbar\omega_0}{eE}. \tag{5}$$

In the following, such a motion in momentum and real space will be referred as OPTTR, a short acronym for optical phonon emission assisted transit-time resonance.

Let us stress that equations (2) and (4) merely describe conditions necessary for the OPTTR realization in momentum space. They are insufficient for the OPTTR to manifest itself in real space as effects directly related with a spatial periodicity of optical phonon emissions by each single carrier (with the period l_0). Spatial manifestation of OPTTR will take place only if there exists a possibility to create, in some restricted region of real space, a carrier stream with the velocity spread

$$\delta v \ll \frac{p_0}{m^*m_0}. \tag{6}$$

Usually, such a condition can be easily realized at the source contact by using, for example, n^+n, n^+n^-n homojunctions with a sharp electric field which prevents carriers from entering into the n-region where the OPTTR conditions are fulfilled. In the case of contacts with a wide velocity spread of entering carriers any spatial effects of the OPTTR will be suppressed.

Under stationary conditions, in momentum space such a cyclic motion leads to the so called *streaming distribution* [1–4], i.e. a carrier distribution elongated along the electric field direction. In real space, the periodic motion of carriers can lead to formation of a free-carrier grating [5–8] and associated kinks in the current–voltage (I–U) characteristics when the applied voltage corresponds to an integer number of optical phonons which can be emitted by a carrier crossing the diode [8].

Under dynamical conditions, such a cyclic motion with the transit-time frequency $f_E = 1/\tau_E$ produces a variety of quite important physical phenomena. For example, the transit-time frequency manifests itself in: (i) damping oscillations of the carrier velocity and energy during a transient response of the carrier ensemble under a step-like switching of the dc electric field [9], (ii) resonant enhancement of the current noise spectrum at a frequency close to f_E [10–12], (iii) a bunching of carriers in momentum space [13–15], (iv) noise upconversion effects [16] under alternating (ac) electric field, etc.

Apart from the above mentioned effects, the most important manifestation of the OPTTR is the possibility of having microwave power generation in the sub-THz and THz frequency regions. As predicted theoretically, such a

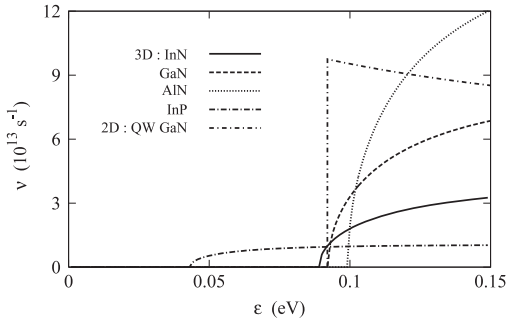

Figure 2. Scattering rate of polar-optical-phonon emission as function of carrier energy in 3D bulk materials and 2D GaN 5 nm QW.

generation can be related to:

(i) the transverse electromagnetic wave amplification in bulk materials [17–20], and
(ii) the longitudinal current instabilities in diode structures [21, 22].

In the former case, the microwave power generation in the frequency range 50–300 GHz was observed experimentally in InP samples by the Vorob'jev group of Saint-Petersburg [23]. In the latter case, a direct observation of the OPTTR induced generation is still absent. However, some manifestations of the OPTTR as kinks at the I–U characteristics were experimentally observed in InSb [24], GaAs [25], InGaAs [26] and InP [27] structures at cryogenic temperatures.

Both the theoretical considerations and the experimental data mentioned above show the possibility of a practical realization of the OPTTR and of its exploitation as a mechanism for generation. Moreover, they indicate the possibility of two different ways to achieve generation near the transit-time frequency. These ways are based on the instability of the transverse electromagnetic waves (analog of quantum laser systems) and longitudinal electrical waves accompanied by the formation of certain spatial structures.

Since the OPTTR frequency $f_E = eE/p_0$ is proportional to the applied dc electric field E, to increase the generation frequency one needs to increase E. For a given material, the increase of E eventually leads to a deterioration in the OPTTR as expressed by condition (4). Therefore, an increase of the OPTTR frequency can be expected in semiconductors with a carrier–phonon interaction stronger than in standard III–V compounds, so that shorter values of τ_+ could be achieved. Such a requirement is satisfied by wide-band nitride materials where the electron–phonon interaction is several times stronger [28] than in standard III–V compounds [29]. This is illustrated by figure 2 which presents the electron scattering rate of optical phonon emission for zincblende InP and wurtzite nitrides.

However, nitride materials in the form of bulk samples are not readily available at the present time. Available samples are mostly n^+nn^+ homostructures and heterostructures with 2D electron transport such as quantum wells (QWs) and heterolayers (HLs). In this context, it is worthwhile emphasizing that transport in 2D exhibits two main advantages with respect to that in 3D, namely: (i) the possibility of increasing the maximum generation frequency because of a more abrupt threshold of the optical phonon emission scattering rate (see figure 2), (ii) the possibility to use high carrier densities whilst avoiding impurity scattering in the passive region due to an increase of τ_-, since donors are usually remotely placed outside the 2D channel.

3. Generation of transverse electromagnetic waves

In this section we shall consider excitation and generation of the transverse electromagnetic waves in bulk nitrides and their 2D channels. It is supposed that the OPTTR conditions are only satisfied in the momentum space and the longitudinal electrical spatial waves are not excited, i.e. the condition given by equation (6) is invalid. The propagation peculiarity of the electromagnetic transverse modes is the absence of interactions with plasma excitations in the semiconductor volume, so that the spatial homogeneity of carrier distribution is not violated. The description of a process of bulk generation for such modes coincides entirely with that of quantum laser systems when the frequency dependence of an amplification coefficient (or dynamic negative differential mobility (DNDM)) of the active medium is supposed to be known. Therefore, here the main attention will be to determine: (i) the frequency regions of generation (i.e. DNDM), (ii) the magnitude of the small- and large-signal amplification coefficient, (iii) the influence of material parameters and external conditions, such as amplitude of the applied dc electric fields, lattice temperature, etc. Estimations of the expected output power and generation efficiency of laser systems based on semiconductor volume in the presence of the DNDM caused by the OPTTR will be given.

The main features of the DNDM under OPTTR conditions will be illustrated by Monte Carlo (MC) calculations performed for nitride-based materials (InN, GaN, AlN). MC simulations of bulk materials include electron scattering by ionized impurities, deformation and piezoelectric acoustic phonons, and polar optical phonons with parameters taken from [28]. The modeling of band structure and scattering mechanisms in 2D QWs and HLs mainly follows [30–33]. For 2D QWs, deformation acoustic and polar optical phonon scatterings are considered [33]. The differential mobility and amplification spectra are calculated in the framework of a small-signal analysis by using averaging over before- and after-scattering ensembles as described in [11, 12, 34]. The characteristic features of generation are calculated in the framework of the large-signal operation as described in [34–36]. To distinguish the electron mobilities obtained under the small- and large-signal operations we shall refer to them as $\mu(f)$ and μ_ω, respectively.

3.1. Dynamic negative differential mobility

In a set of pioneering papers [17–20], it was predicted that, under the fulfillment of the OPTTR conditions (2) and (4), by superimposing a small ac field to a high dc field the oscillating dynamics leads to a carrier bunching in momentum space. The corresponding negative phase shift $\varphi > \pi/2$, with respect to the ac electric field, can produce DNDM near the

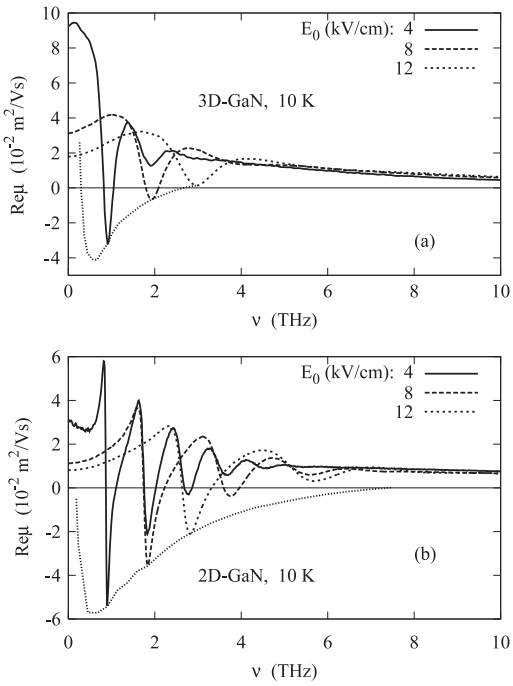

Figure 3. Real part of the differential mobility spectrum calculated by the Monte Carlo method for GaN: (a) bulk material, and (b) 5 nm QW structure. The dotted lines refer to the maximum value of the DNDM as a function of frequency.

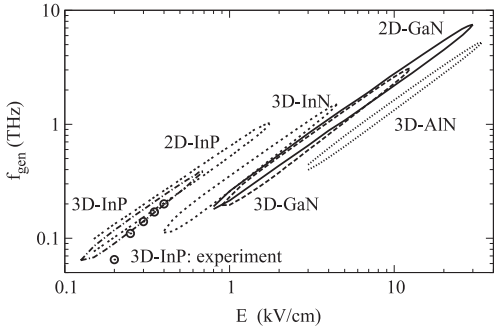

Figure 4. Generation bands (frequency regions where the real part of the differential mobility is negative) as a function of applied dc field calculated by Monte Carlo method for bulk materials as well as 12 nm InP and 5 nm GaN QW structures at 10 K. Points refer to the generation frequency obtained experimentally by Vorob'ev *et al* [23].

OPTTR frequency due to:

(i) the forward directional character of *polar* optical phonon emission in momentum space,
(ii) the decrease, with electron energy increase, of the scattering rate in the passive region, as it takes place for ionized impurity and piezoelectric phonon scattering (assuming the validity of the condition expressed by (2)).

To illustrate the general trends of the DNDM behavior in 3D materials and 2D structures, figure 3 shows the real part of the differential mobility spectrum, $\mathrm{Re}[\mu(f)]$, calculated by the MC method for bulk GaN with a donor concentration $N_\mathrm{D} = 10^{16}$ cm^{-3} and 5 nm GaN QW (figures 3(a) and (b), respectively) at the same values of the applied dc electric field. As follows from figure 3, the general behavior of the mobility spectrum is the same in both 3D and 2D cases. The OPTTR manifests itself as a series of $\mathrm{Re}[\mu(f)]$ minima at the transit-time frequency and its higher harmonics. Negative values of $\mathrm{Re}[\mu(f)]$ (that is the DNDM) correspond to frequency regions where amplification and generation is possible (the so called generation bands). The magnitude of the first DNDM minimum at the resonant frequency as a function of the applied dc field E is given by the dotted lines that illustrate the total frequency range of possible amplification/generation for the given material or 2D structure.

Figure 4 summarizes the state-of-the-art and compares results of MC simulations of the OPTTR generation frequency band as function of the applied dc field for various 3D [34–39] and 2D [33, 40, 41] semiconductor structures. Points show the generation frequency obtained experimentally by Vorob'ev *et al* [23] in InP 54 mm × 8 mm × 7 mm samples in the geometry corresponding to the transverse electromagnetic waves generation. The low-frequency cutoff of generation (lower ends of the generation bands in figure 4 and left wing of the dotted lines in figure 3) is related to the violation of the quasi-ballistic motion of electrons in the passive region (equation (2)). The high-frequency cutoff (upper ends of the generation bands in figure 4 and right wing of the dotted lines in figure 3) is related to the increasing penetration of electrons into the active region (equation (4)). As evident from figure 4, the electric field regions and, hence, the generation bands cover a rather wide frequency range, which strongly depends on semiconductor material and transport type (2D or 3D). Furthermore, all the generation bands exhibit a similar behavior, thus indicating the existence of some general rules at the basis of their formation.

An universal description of the OPTTR assisted generation band for sub-THz and THz radiation was developed in [33] in the framework of a 3D transport in bulk materials and 2D transport in QWs and HLs. The model is based on quantitative estimations of the qualitative constraints given by conditions (2) and (3) for the streaming conditions obtained from numerical calculations of the OPTTR DNDM by MC simulations performed for different bulk materials and 2D structures. It was found that:

(i) the low-frequency (LF) cutoff of the DNDM at OPTTR takes place when the average momentum relaxation rate in the passive region $1/\tau_-$, which includes all the scatterings, increases up to critical values comparable with the transit-time frequency f_E:

$$\frac{1}{\tau_-} \sim f_E \begin{cases} 1/2, & \text{3D} \\ 1, & \text{2D.} \end{cases} \tag{7}$$

(ii) independently of 3D or 2D transport type, the high-frequency (HF) cutoff appears at the same value of average penetration depth

$$\langle \delta\varepsilon \rangle_\mathrm{cut} \approx (0.14\text{–}0.15)\hbar\omega_0. \tag{8}$$

As a consequence, for the HF cutoff of the DNDM it was found that:

(i) in going from 3D to 2D transport, for the same material the change of the energy dependence of the density-of-states is responsible of an extension of the maximum generation frequency for up to a factor of five times.
(ii) the effective constant of polar optical (po) phonon emission scattering rate given by:

$$\Lambda_{\rm po} = \frac{e^2(\hbar\omega_0 2m_0 m^*)^{1/2}}{4\pi\hbar^2\kappa_0}\left[\frac{1}{\kappa_\infty} - \frac{1}{\kappa_{\rm s}}\right] \tag{9}$$

with κ_0 the vacuum permittivity and $\kappa_{\rm s}$, κ_∞ the static and high-frequency relative dielectric constant, respectively, allows one to provide an universal presentation of the generation band associated with the OPTTR for various 3D materials and their 2D structures on the basis of some relevant physical quantities, namely: the carrier effective mass, the optical phonon energy, and the po coupling strength.

Figure 5 reports the results of available calculations and experiments for various bulk materials and 2D structures already shown in figure 4 in terms of universal material-independent generation bands. Such a universal representation is obtained when the electric field E and the generation frequency $f_{\rm gen}$ are normalized, respectively, to the effective electric field of po-phonon emission

$$E^i_{\rm po} = \frac{1}{e}p_0\nu^i_{\rm po} \tag{10}$$

and the po-phonon effective scattering rate given by:

$$\nu^i_{\rm po} = \begin{cases} \Lambda_{\rm po}, & i = 3{\rm D} \\ \Lambda_{\rm po}G^{\rm 2D}_{\rm po}(\varepsilon = \hbar\omega_0), & i = 2{\rm D} \end{cases} \tag{11}$$

where the second line in equation (11) simply gives the po-phonon emission scattering rate at $\varepsilon = \hbar\omega_0$ (see [33] for more details). As follows from figure 5, such an approach allows us to reduce the variety of calculations presented in figure 4 to the two main cases of 3D and 2D transport, respectively. Such a unified description provides an effective way for a simple estimation of possible generation bands in the case of 3D and 2D transport in various materials.

In essence, the model developed in [33] gives the 'upper' estimate of the HF-limit of the generation band primarily determined by the parameters of a bulk material and a 2D structure. For the LF-limit, equation (7) gives a reasonable estimate by supposing that all low-energy scattering rates are incorporated into an average momentum relaxation time in the passive region τ_- as $1/\tau_- = 1/\tau_{da} + 1/\tau_{\rm imp} + 1/\tau_{ee}$. For example, such a procedure was used to estimate τ_- in the experimental observation of the OPTTR generation in bulk InP [23]. These estimations give $\tau_- \approx \tau_E$ which is reasonably close to the values estimated above.

In concluding this subsection let us note that more detailed MC results on the DNDM induced by OPTTR and associated features can be found in [11, 12, 33–39, 46] for the 3D case and [33, 40–46] for the 2D case.

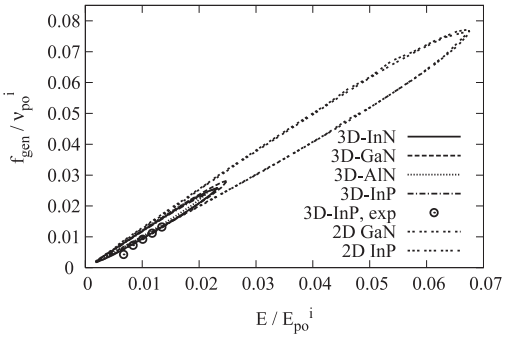

Figure 5. The same dependences as in figure 4 but normalized to the characteristic po-scattering field $E^i_{\rm po}$ and frequency $\nu^i_{\rm po}$ defined by equations (10) and (11), respectively.

3.2. Amplification and generation

It is worthwhile describing the feasibility of an active medium (in our case a bulk semiconductor or a 2D layer in the presence of DNDM induced by OPTTR) amplifying and generating transverse electromagnetic waves in terms of the so called static and dynamic amplification coefficient (gain) which, for the single-mode operation, is given by [47, 48]:

$$\alpha_\omega(U_\omega) = -\frac{\sqrt{\kappa_{\rm s}}}{c}\frac{P_\omega(U_\omega)}{U_\omega} \tag{12}$$

where U_ω is the single-mode radiation energy density inside the volume of the active media under test, $P_\omega(U_\omega)$ the generated (or absorbed) radiation power density, c the light velocity in vacuum, f the frequency of single-mode radiation, $\omega = 2\pi f$ the cyclic frequency. The radiation energy density U_ω can be written as:

$$U_\omega = \frac{1}{T_\omega}\int_0^{T_\omega} \kappa_0\kappa_{\rm s}|E(t)|^2\,{\rm d}t \tag{13}$$

where $E(t) = {\rm Re}[E_\omega \exp({\rm i}\omega t)]$ is the microwave (MW) electric field, and $T_\omega = 2\pi/\omega = 1/f$ the period of the MW electric field. In turn, the power density generated by the active medium is given by:

$$P_\omega = \frac{1}{T_\omega}\int_0^{T_\omega} en\langle v(t)\rangle E(t)\,{\rm d}t \tag{14}$$

where n is the free-carrier concentration, and $\langle v(t)\rangle$ the average drift velocity during a period of the MW field. According to its definition, P_ω takes negative values in the region of generation, so that the dynamic gain is positive in this case. Substitution of equations (13) and (14) into equation (12) yields the amplification coefficient in its conventional form:

$$\alpha_\omega = -\,{\rm Re}[\mu_\omega]n\frac{e}{c\kappa_0\sqrt{\kappa_{\rm s}}} \tag{15}$$

where ${\rm Re}[\mu_\omega] = 2P_\omega/enE^2_\omega$ is the real part of the carrier MW mobility which takes negative values under generation conditions. Notice that equations (12) and (15) are general and hold true for both linear and nonlinear regimes of the MW radiation interacting with the medium.

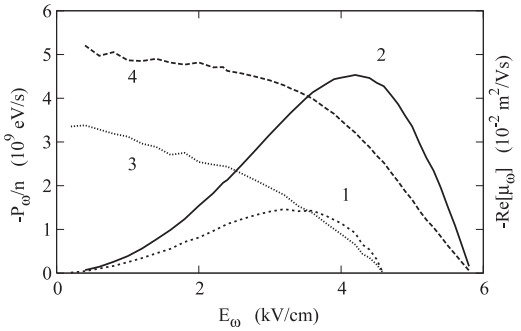

Figure 6. Generated power (curves 1, 2) and dynamical mobility (curves 3, 4) calculated for bulk GaN with a donor concentration $N_D = 10^{16}$ cm^{-3} (1, 3) and GaN 5 nm QW (2, 4) as functions of the microwave electric field amplitude E_ω at frequency $f = 1$ THz superimposed on a dc electric field $E_0 = 4.35$ kV cm^{-1} applied to the samples.

Under linear operation conditions, when $U_\omega \to 0$, both α_ω and Re[μ_ω] are independent of U_ω, so that, analogous to the previous subsection, we shall label them as α and Re[μ]. In this case the static gain: (i) determines the frequency region of amplification, (ii) estimates a threshold value for the net losses at which the generation is still possible, (iii) allows one to choose the optimal concentration n for a given sample, etc.

Under nonlinear operation conditions, both α_ω and Re[μ_ω] depend on U_ω (or E_ω). Typically, for any active medium an external resonant system will lead to the onset and growth of a MW field amplitude E_ω inside the active medium. At the initial stage, determined by the static gain, such a growth of E_ω will lead to an increase of the microwave power P_ω proportional to Re[μ_ω]E_ω^2. However, a considerable increase of E_ω will result in a decrease of the dynamical gain due to the suppression of the physical mechanism responsible for DNDM. Finally, the complete disappearance of the amplification effect will take place at sufficiently high E_ω when both the gain and the generated power go down to zero. Such a behavior is illustrated in figure 6, which presents MC simulations of the generated power normalized to one free-carrier P_ω/n (curves 1, 2) and large-signal mobility Re[μ_ω] (curves 3, 4). Curves 1, 3 and 2, 4 refer to bulk GaN and GaN 5 nm QW structure. All parameters ($f = 1$ THz, $E_0 = 4.35$ kV cm^{-1}, $T = 10$ K, etc) correspond to the first DNDM minimum shown in figures 3(a) and (b). As follows from figure 6, with the increase of E_ω the generated power starts from zero, reaches a maximum at some optimum value of the MW field amplitude, and finally goes to zero at the highest values of the MW field amplitude. In turn, the large-signal mobility starts from values predicted by the linear theory (see figure 3) and then monotonically goes to zero. One can see that the large-signal behavior is similar for both bulk materials and quantum structures.

The nonlinear behavior allows us to consider the generation process on the basis of the energy balance among the generated, absorbed, and extracted radiation powers [34–36]. The stability of the generation process implies that all radiation losses are exactly compensated by the radiation amplification due to DNDM inside the system. Therefore, under stable generation of the single-mode radiation, the dynamic gain is equal to the coefficient of the net loss in the resonant system,

$$\alpha_L = \Gamma + \Lambda. \tag{16}$$

This coefficient includes both the outside power extraction, as described by the coefficient coupling the active medium with the external free space, Γ, and all the parasitic losses in the resonant system, as described by the coefficient of internal losses, Λ. Therefore, one can finally represent the power generated inside the resonator as a function of α_L by:

$$P_{gen}(\alpha_L) = -P_\omega(\alpha_\omega). \tag{17}$$

The simulation of the nonlinear response allows us to obtain the function $P_\omega(U_\omega)$ and to calculate $\alpha_\omega(U_\omega)$ in accordance with equation (12). Then, by eliminating U_ω from $P_\omega(U_\omega)$ and $\alpha_\omega(U_\omega)$, that is, by expressing P_ω as a function of α_ω, one obtains the dependence of the output power extracted from the OPTTR maser upon the generalized parameters of the resonator:

$$P_{out} = P_{gen}(\alpha_L)\frac{\Gamma}{\Gamma + \Lambda}. \tag{18}$$

We conclude that the dependence of the generated power on the dynamic gain obtained from equations (16)–(18) allows us to estimate: on one hand, an upper limit of the output generated power and, on the other hand, its dependence on the generalized parameters of the resonant circuit, namely: Γ and Λ. We stress that the general behavior of the static and dynamic gains with the variation of free-carrier concentration already directly follows from equations (14) and (15). Both the gain and the generated power should increase with the increase of the carrier concentration controlled by the doping level. However, the increase of the carrier concentration in turn decreases the value of $-$Re[μ_ω], and hence, of both α_ω and P_ω, due to ionized impurity [34] and electron–electron [44] scattering. The competition between these two opposing tendencies implies the existence of an optimum range of doping level for each generation frequency where the gain and the generated power are maxima.

3.2.1. Small-signal operation. Figure 7 presents the gain $\alpha(f, n)$ and the real part of the differential mobility, Re[$\mu(f, n)$], in the upper and lower parts of the figure, respectively, as a function of the electron concentration n at four fixed frequencies of $f = 0.25, 0.5, 1$, and 1.5 THz (curves 1–4) at $T = 10$ K calculated for GaN. As can be seen from figure 7, in full agreement with equation (15) at low level of electron concentration, the DNDM is practically constant (or even slightly increases due to the constructive role of ionized impurity scattering) while the gain grows practically linearly with n. At increasing carrier concentration, the gain reaches a maximum and then decreases to zero due to the decrease of the DNDM caused by the destructive role of ionized impurity scattering at high level of doping. In so doing, the value of the possible maximum gain remains fairly constant, $\alpha =$ 100–150 cm^{-1}, over a wide frequency range. By contrast, the optimum doping level is found to strongly depend on

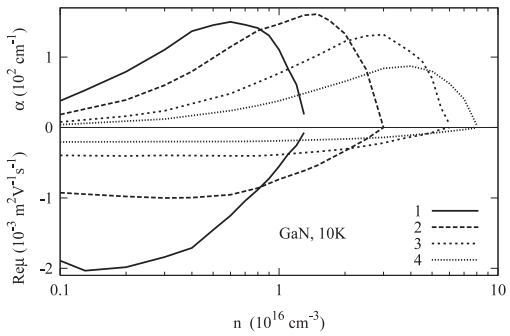

Figure 7. Real part of differential mobility (lower curves) and gain (upper curves) as function of electron concentration in 3D GaN at $f = 0.25, 0.5, 1, 1.5$ THz for $T = 10$ K (curves 1–4).

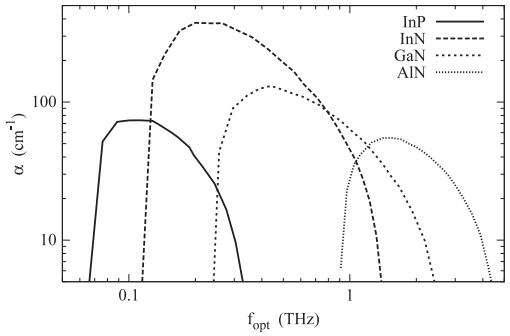

Figure 8. Amplification coefficient as function of the optimum frequency calculated by the Monte Carlo method for InP and nitride materials. The carrier concentration is chosen to get the maximum values of α at $T = 10$ K.

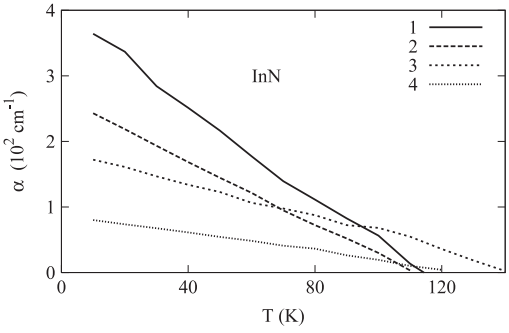

Figure 9. Temperature dependence of the small-signal gain α at frequencies $f = 0.25$ THz calculated for InN with $n = 10^{16}$ cm^{-3} (curve 1) and $f = 0.5, 0.75, 1$ THz for $n = 3 \times 10^{16}$ cm^{-3} (curves 2–4).

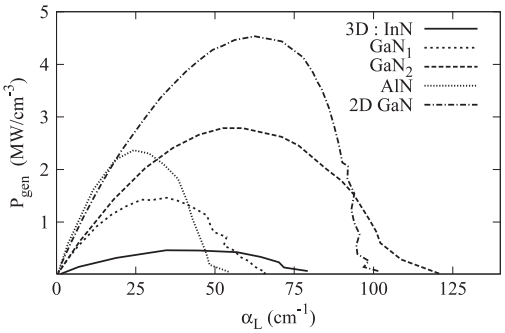

Figure 10. Generated power at frequency 1 THz as a function of the coefficient of total losses inside the resonator, α_L, calculated for bulk InN ($N_D = 10^{16}$ cm^{-3}, $E_0 = 2.4$ kV cm^{-1}), GaN ($N_D = 1$ and 2×10^{16} cm^{-3}, $E_0 = 4.35$ kV cm^{-1}), AlN ($N_D = 10 \times 10^{16}$ cm^{-3}, $E_0 = 20$ kV cm^{-1}), and GaN 5 nm QW ($N_D = 10^{16}$ cm^{-3}, $E_0 = 4.35$ kV cm^{-1}).

frequency. As illustrated by figure 7 and confirmed by MC calculations for other bulk materials, the optimum doping level strongly depends on the desired frequency and differs by about one order of magnitude in going from the left to the right wings of the amplification band for the same material.

Figure 8 summarizes the amplification coefficients as a function of the generation frequency calculated for InP, InN, GaN and AlN with a carrier concentration chosen to maximize the values of $\alpha(f, n)$ of, respectively, $n = 0.1, 1, 1, 6 \times 10^{16}$ cm^{-3}. As follows from figure 8, sufficiently high values of gain can be achieved in a wide frequency range for bulk InP and nitrides. As a general trend, the maximum values of the gain are obtained for InN (300–400 cm^{-1}) with respect to GaN (100–150 cm^{-1}) and AlN (50–60 cm^{-1}).

The increase of the lattice temperature always leads to a decrease of both the DNDM and the amplification coefficient due to the increase of the scattering intensity in the passive region. This is illustrated in figure 9, which presents the variation of α with temperature in InN at different frequencies. The wide temperature range of amplification offers favorable conditions to obtain generation experimentally at both liquid helium and liquid nitrogen temperatures.

3.2.2. Power generation and efficiency. Figure 10 presents the generated power at 1 THz as a function of the coefficient of total losses inside the resonator, α_L, calculated for bulk nitrides and a GaN 5 nm QW structure. For the 2D case we have used the characteristics reported in figure 6 and recalculated for $N_D = 10^{16}$ cm^{-3}. Let us recall that for a stable generation the dynamical gain must exactly compensate all the losses in the resonant system due to power extraction outside the resonator, parasitic, etc, i.e. $\alpha_\omega = \alpha_L$. Accordingly, if at a given frequency α_L exceeds the small-signal gain, $\alpha(f)$, given by the linear theory (see, e.g., figures 3 and 7), then any generation is absent. Therefore, with a decrease of α_L, at each given frequency (1 THz in the case of figure 10) generation starts from the value of the small-signal gain. With a subsequent decrease of α_L, the power increases and reaches a maximum value at the optimum amplitude of the MW field. As follows from figure 10, this optimum value is achieved when $\alpha_L \simeq 0.5\alpha_\omega^0$. Here, a generation efficiency of about 1–2% (up to 4% for the QW) is achieved. With a further decrease of α_L, the amplitude of the MW field increases so much that it would destroy the transit-time resonance. For this reason, the generated power decreases to finally vanish at $\alpha_L = 0$.

4. Longitudinal current instabilities in n^+nn^+ diodes

In this section we shall consider another possible kind of instability induced by OPTTR, namely: excitation of

longitudinal electrical waves that are directly related to collective plasma effects. Such a kind of instability is caused by the periodic process in real space (determined by the distance $l_0 = \hbar\omega_0/eE$, see equation (5)) induced by the periodic stopping of the moving carriers, occurring after successive emissions of optical phonons, with a carrier injection from the source contact which satisfies the condition given by equation (6).

Let us recall that for the instability onset the phase shift between drift current fluctuations and the electric field, φ, which produces these fluctuations, must satisfy the condition $\varphi > \pi/2$. Here, such a shift is formed by processes that are induced by a collective plasma interaction in real space, rather than in momentum space as takes place for the transverse instability where a necessary condition is the forward peaked probability of polar optical phonon scattering. Therefore, in principle longitudinal instabilities induced by the OPTTR can take place independently of the polar or nonpolar (deformation potential) character of optical phonon scattering. This opens another possibility to realize OPTTR assisted instabilities along the direction of the applied field in various n^+nn^+ structures in terms of current instabilities. As a general trend, a comprehensive investigation of such instabilities was carried out in two cases on n^+nn^+ structures with 3D transport.

The first case refers to n^+nn^+ structures with a short n-region of length d comparable with that of a free-flight, i.e. $d \approx l_0$. Here, each electron crosses practically the whole n-region almost ballistically with the possibility of emitting an optical phonon just before entering the opposite contact. As predicted by Ryzhii *et al* [21, 22], these conditions are favorable for the onset of an instability leading to sub-THz and THz radiation generation [49, 50].

The second case refers to n^+nn^+ structures with long n-regions with characteristic lengths $d \approx (10\text{–}20)l_0$ (up to about 20 μm) where each electron crossing the n-region of the structure emits a large number of optical phonons. In this case, as shown in [5–8], there is a possibility of forming a spatial modulation with period l_0 of the electron concentration and related quantities, the so called dynamic free-carrier superlattice or grating. Moreover, under certain conditions, the dynamical gratings become unstable, which can lead to generation in the THz frequency range.

In the following, the two cases seen above and the transition between them are investigated by MC simulations in n^+nn^+ InN structures. Numerical calculations of electron transport are performed by a simultaneous solution of the coupled Boltzmann and Poisson equations through an ensemble MC technique [51]. To simulate THz generation, these equations are solved together with the equations appropriate to the external resonant circuit as detailed in [52].

4.1. Ryzhii instability

Under the condition of constant voltage applied to the structure terminals, such as $u_0 < U < 2u_0$, with $u_0 = \hbar\omega_0/e$, the instability predicted in [21, 22] manifests itself as current oscillations and can be explained qualitatively as follows. Cold electrons with average energy $\langle\varepsilon\rangle \ll \hbar\omega_0$ are injected from the emitter (left n^+-region). After being accelerated by the electric field up to the energy $\hbar\omega_0$, they are stopped by emitting optical phonons and then undergo a new acceleration. The stopping point subdivides the n-region into two zones, namely, the zone from the emitter to the stopping point and that from the stopping point to the collector (the right n^+-region). These two zones, which usually have different lengths (the left being longer than the right) cannot conduct the same current. This leads to a space charge accumulation in the n-region near to the stopping place and, as a consequence, to a suppression of electron injection from the emitter. Once the electron excess charge is extracted by the collector the process is repeated.

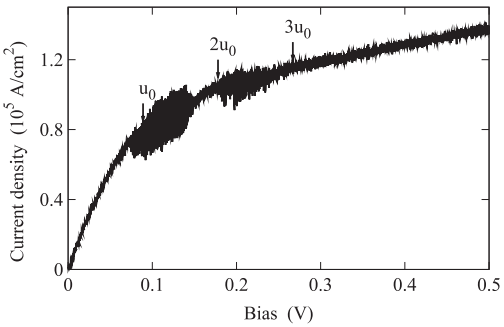

Figure 11. Simulated current–voltage characteristics of 0.02–0.05–0.3–0.02 μm $n^+n^-nn^+$ InN structure at 80 K under voltage driven operation. $n^- = 5 \times 10^{15}$ cm^{-3}, $n = 3 \times 10^{16}$ cm^{-3}, $n^+ = 10^{18}$ cm^{-3}.

Figure 11 reports the I–U characteristic (with I expressed in units of current density) of an InN structure optimized to exhibit maximum power generation in the THz frequency range at $T = 80$ K. Here, the enhanced spread of the characteristic, due to nearly-harmonic current oscillations, is associated with different instability zones. The first instability zone at $u_0 < U < 2u_0$ is a direct consequence of the Ryzhii effect [21, 22] when an electron crossing the n-region emits only one optical phonon. In the successive instability zone at about $2u_0 < U < 3u_0$ an electron emits two optical phonons while crossing the n-region and the physical consequence will be discussed in section 4.2.

Figure 12 reports the generated power and efficiency spectra for the first instability zone of figure 11. Results are obtained by MC simulations of the performance of the structure coupled to a parallel resonant circuit. The arrow indicates the current oscillation frequency f_0 of the structure operating without the external circuit when the amplitude of the self-oscillations is near to its maximum. Such a frequency corresponds to the transit-time frequency of the bulk material, f_E, under the condition that the optical phonon emission occurs at a position of about 0.7–0.8 times the total n-region length, which is consistent with the results of [53]. The maximum power is generated at frequencies below f_0, which is also typical for longitudinal instabilities (see, e.g., [54]).

As shown by the previous MC simulations, and also found in similar $n^+n^-nn^+$ InN structures [49, 50] optimized for 1 THz generation, MW power generation at 80 K is possible in the frequency range 0.9–1.5 THz. These structures, when coupled to a parallel resonant circuit, at 80 K can generate up

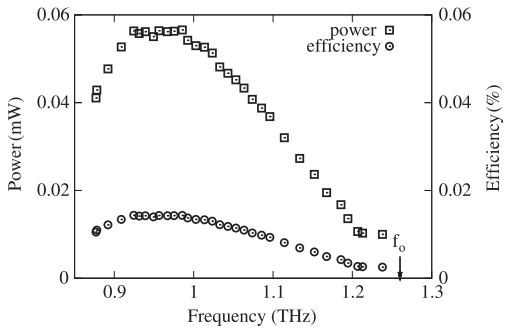

Figure 12. Generated power and efficiency spectra of the $n^+n^-nn^+$ InN structure of figure 11 operating in a parallel resonant circuit at 80 K.

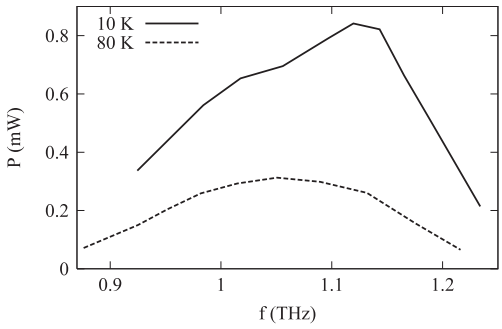

Figure 14. Generated power spectra of a 3 μm n^+nn^+ InN diode with $N_D = 2.2 \times 10^{16}$ cm^{-3} operating in a parallel resonant circuit at 10 and 80 K, respectively.

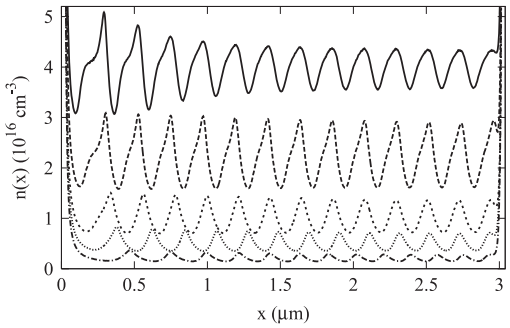

Figure 13. Concentration profiles in the n-region of an n^+nn^+ InN structure at 80 K and $U = 1.2$ V for different dopings n of the n-region: curves from bottom to top correspond to $n = 0.2$, 0.5, 1, 2.2, and 4×10^{16} cm^{-3}. $n^+ = 10^{18}$ cm^{-3}.

to 100 μW power within the 0.9–1.2 THz frequency range. The simulations of power generation near to 1 THz show that generation remains possible up to temperatures of about 150 K and specific contact resistances of 5–10 $\times$ 10^{-6} Ω cm^2. These circumstances point to an experimental validation of the suggested MW power generation in the THz frequency range.

4.2. Dynamic free-carrier grating

In long n^+nn^+ structures, electrons crossing the n-region can exploit the possibility of multiple emissions of optical phonons, i.e. multiple entire stops. As shown in [5–8] in such a case the formation of a dynamical spatial superlattice (grating) in the n-region becomes possible. This phenomenon is illustrated in figure 13, which reports the spatial profiles of the electron concentration $n(x)$ in the n-region of an n^+nn^+ InN structure at $T = 80$ K. Similarly to the single-phonon emission case considered above, cold electrons with $\langle\varepsilon\rangle \ll \hbar\omega_0$ are injected from the emitter into the n-region. They are accelerated by the field up to the optical phonon energy and then practically stop after optical phonon emission. However, since the applied voltage is high enough to establish a multiple optical phonon emission regime, this process is repeated in real space until the electron leaves the n-region through the collector. The stopping places coincide with a maximum of carrier concentration, and their number is the integer part of the ratio $eU/\hbar\omega_0$. Therefore, we observe the formation of a free-carrier grating with period $l_0 = \hbar\omega_0/e\bar{E}$, where $\bar{E} \approx U/L$ is the average field in the n-region. As shown in [5–7], under such conditions the electron transport through the whole n-region can be considered as the transport through a series connection of short n^+nn^+ substructures of length l_0, where the stopping place serves simultaneously as the emitter and collector of two neighboring substructures.

We notice that, at increasing voltages, the appearance of a new period for the grating occurs abruptly when the voltage drop at the n-region of the diode, U_n, is equal to an integer number of $\hbar\omega_0$, i.e., $U_n = k\hbar\omega_0$ where $k = 1, 2, 3, \ldots$. The step-like formation of a new period is reflected in the static I–U characteristic of the diode as small periodic kinks of period $\Delta U = \hbar\omega_0$, accompanied by oscillations of its derivative, $\mathrm{d}I/\mathrm{d}U$, with an increase of the applied voltage [8, 46]. We stress, that such a behavior of $I(U)$ and $\mathrm{d}I/\mathrm{d}U$ serves as an experimental confirmation of the existence of a free-carrier grating. For example, such oscillations were experimentally observed in InSb, GaAs, InGaAs, and InP structures at cryogenic temperatures [24–27], however, in these works there were no attempts to relate them to the grating formation. Several MC simulations [5–8] show that such spatial gratings can be subdivided into two types: stable and unstable gratings. For the first type, the structures formed in space and the current flowing through the structure are stationary in time. For the second type, the grating is 'breathing' in time so that the current undergoes periodic or near-periodic oscillations in time. The breathing grating can be treated as a manifestation of the Ryzhii instability [21, 22] extended to the case of more than a single stop (optical phonon emission) in the n-region. As follows from figure 11, with an increase of the number of optical phonon emission events the self-oscillation amplitude decreases significantly. Here, current oscillations practically lose their harmonic character and their time dependence becomes noisy. Nevertheless, even in these conditions THz power generation becomes possible provided the n^+nn^+ structure is embedded into an external resonant circuit. This is illustrated in figure 14, which reports the frequency dependence of the THz power generated by the InN diode shown in figure 13 (with a n-region doping of $N_D = 2.2 \times 10^{16}$ cm^{-3}) connected with a parallel resonant circuit.

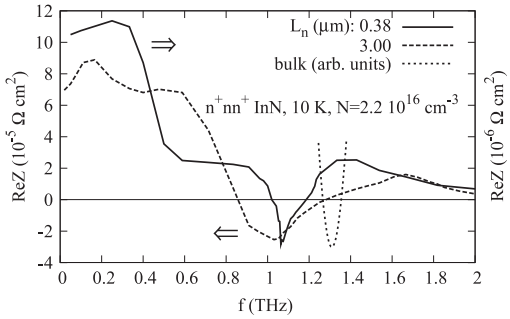

Figure 15. Real part of small-signal impedance of sub-micron and micron InN n^+nn^+ diodes (solid and long-dashed curves, respectively) as function of frequency calculated by an ensemble Monte Carlo technique. For comparison, short-dashed curve shows the minimum of Re$[\mu(f)]$ (in arbitrary units) calculated by the Monte Carlo method for a bulk material. For all the curves the average electric field is 4 kV cm^{-1}.

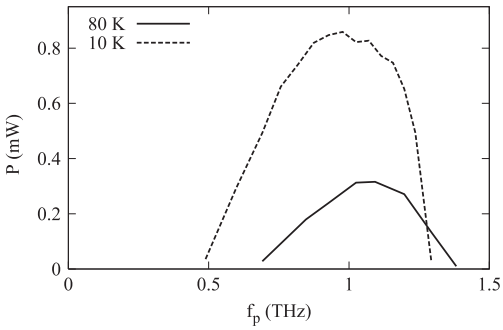

Figure 16. Dependence of generated power on n-region plasma frequency (determined by its doping as $f_p = (\sqrt{e^2n/\kappa\kappa_0 m^*})/2\pi$) calculated by an ensemble Monte Carlo technique for a 3 μm n^+nn^+ InN structure operating in a parallel resonant circuit at 10 and 80 K, and given frequencies $f = 1.14$ and 1.05 THz, respectively.

To investigate the effect of temperature, figure 14 reports the spectra of the generated power for an InN diode calculated at $T = 10$ and 80 K, respectively. Simulations show that at 10 K the generated power considerably exceeds that generated at 80 K due to the smaller level of acoustic scattering intensity in the passive region. By comparing figure 14 with figure 12 a considerable increase of the generated power is seen. This is due to the fact that a long diode in the presence of a free-carrier grating can be considered as a chain of series connected shorter subdiodes with single-optical phonon emission. Accordingly, the total generation power of the grating is practically that of a single subdiode multiplied by the number of subdiodes. It is worthwhile emphasizing that the longitudinal instabilities in the presence of OPTTR conditions considered here are the result of the coupling of two physical processes, namely:

(i) the cyclic dynamics of electrons in the passive region of momentum space, i.e. OPTTR, and
(ii) the collective plasma interaction of electrons in real space, which provides the synchronization of the fluctuations coming from the current and from the self-consistent electric field, which is necessary for the appearance of current instabilities.

The presence of this coupling of physical processes is illustrated by figures 15 and 16. Figure 15 reports the real part of the small-signal impedance, Re$[Z(f)]$, calculated by an ensemble MC procedure for short and long n^+nn^+ InN diodes. In both cases negative values of Re$[Z(f)]$ appear in the same frequency range placed slightly below the DNDM minimum of bulk InN. This clearly indicates the same origin of the longitudinal current instabilities induced by the OPTTR in both sub-micron and micron diodes.

Figure 16 reports the generated power calculated by an ensemble MC procedure as a function of the n-region plasma frequency for a resonant-circuit-operation of the 3 μm n^+nn^+ InN structure with various doping levels. The maximum generated power is extracted when the transit-time frequency is near to the plasma frequency. This result shows that the negative shift, $\varphi > \pi/2$, between the MW component of the current and field, which is necessary for the appearance of the longitudinal current instabilities and generation, takes maximum values when the transit-time and plasma frequency are nearly equal.

5. Conclusions

Summarizing this review, we conclude that optical phonon emission assisted transit-time resonance (OPTTR) of carriers in momentum and real spaces provides a unique possibility to realize sub-THz and THz radiation generation at the border of the electro-optical and electronic techniques by exploiting both these techniques. On one hand, analogously with lasing technologies, the amplification and generation of transverse electromagnetic waves in bulk (or bulk-like) samples can be realized, as was experimentally verified by Vorob'ev *et al* [23]. On the other hand, analogously with micron and sub-micron structures, microwave and THz power generation can be obtained from longitudinal current instabilities similar to those analyzed by Ryzhii *et al* [21, 22]. It should be emphasized that both possibilities are closely related to the *dynamic* character of the hot-carrier negative small-signal conductivity induced by OPTTR. An additional advantage of OPTTR is that the generation frequency can be easily tuned in a sufficiently wide frequency range by changing only the strength of the applied electric field.

The results of numerical simulations show that with respect to standard semiconductor A_3B_5 compounds the nitride-based materials offer the following interesting possibilities:

(i) to expand the generation spectrum up to 3–5 THz, since the maximum values of constant applied field at which DNDM is still possible can be increased considerably;
(ii) to reach sufficiently high values of the amplification coefficient and generated power, due to the possible increase of the optimum doping level up to impurity concentrations of $N_D = 2$–4×10^{16} cm^{-3};
(iii) to expand the range of the working temperature from cryogenic up to the liquid nitrogen value (at least for InN and GaN), which considerably simplifies the experimental implementation of OPTTR.

As concerns THz radiation generation due to OPTTR, the GaN-based structures seem to be the most preferable at the present time. On one hand, even a bulk-like 3D electron transport in epilayers is of great interest, by supposing that propagation (and amplification) of transverse electromagnetic waves can be realized inside the same epilayer. On the other hand, one can exploit the transition from 3D to 2D transport in advanced AlGaN/GaN heterostructures, which provides a considerable increase of the maximum generation frequency. It should be stressed, that the increase of the high-frequency cutoff in 2D structures means, in essence, the possibility by increasing the dc electric field to ease considerably the critical factors at the basis of OPTTR realization, and which are related with the lattice temperature, impurity concentration, etc. This is very important for the generation mechanisms that are assisted by OPTTR in micron and sub-micron n^+nn^+ 3D structures where, due to OPTTR interaction with plasma oscillations, the conditions for THz generation are easier than those in 3D homogeneous structures. For example, as seen above, in InN n^+nn^+ structures THz generation can persist up to temperatures of 100–140 K [49]. For such structures the transition to a 2D transport could lead to an additional extension of the temperature range, hopefully up to room temperatures.

Unfortunately, it is necessary to stress that the experimental investigation of the effects related with OPTTR suffers from a considerable time-lag with respect to the theoretical predictions developed so far, and which have been summarized in the present review. The reasons of such a lag can be of a subjective as well a objective nature. Within the subjective reasons, on one hand, we mention the fact that to date OPTTR effects do not represent an 'hot-topic' in physical research since they are based on sufficiently well-established physical phenomena known for the last 30–35 years. On the other hand, these investigations cannot be treated as only related to THz amplification/generation. Indeed, in full analogy with the development of hot-carrier lasers and masers [1] such a study must include a large variety of experimental investigations, such as low-field mobility, contacts (ohmic and non-ohmic) and their characteristics, high-frequency intrinsic noise (luminescence), resonant systems, etc.

The objective reasons are related to the fact that all existing experiments concerning the OPTTR were obtained in bulk A_3B_5 materials developed with good technology of production, reliable control of the involved parameters and contacts, etc. Indeed, an experimental validation of the OPTTR assisted microwave radiation/generation was obtained only for the case of sufficiently long InP samples(about 5–10 cm) and with Ohmic contacts [23]. At the present time, bulk samples of nitrides with sufficiently large size are practically non-existent. The only available samples are mostly n^+nn^+ micron and sub-micron structures, nanolayers with 2D transport, and similar structures. The electrical characteristics of these structures and layers depend on a variety of parameters, related to the technological process, some of which are not well controlled. In such conditions, the selection of samples appropriate for the realization of THz radiation amplification/generation due to OPTTR implies a large variety of complementary investigations, which include the characteristics of electron transport (low-field mobility and carrier concentration), contact resistance, amplification coefficient, etc. To this end, we believe that a very important step should be that of investigating OPTTR accompanying effects that allow the identification of the realization of transit-time dynamics in momentum and real spaces under conditions more relaxed than those necessary for the generation induced by OPTTR alone.

In this context let us stress that, apart from MW radiation amplification and generation, the noise behavior under OPTTR conditions is of importance since it also reflects the cyclic dynamics of electrons in momentum space and, hence, it can serve as a precursor indicator of an instability. Moreover, it is usually easier to perform measurements of spontaneous radiation (noise) rather than to achieve radiation from stimulated generation with the sample placed inside some external resonance system. For example, recent experimental techniques allow one to measure the current noise spectrum in the THz frequency range even at liquid helium temperatures (see, e.g. [55] and references therein).

Finally we mention the interesting possibility of experimentally verifying the OPTTR quality and the appearance of spatial free-carrier gratings from the measurements of peculiar features of the current–voltage characteristics in n^+nn^+ and similar structures.

Acknowledgments

This work is supported by the Lithuanian State Science and Studies Foundation contracts Nos P-01/2007 and V-08023, bilateral French-Lithuanian programme Gilibert EGIDE, the bilateral Italian-French project Galileo 2007–2008 and the project AITHER BLAN07-3-185228 supported by French ANR (Agence Nationale de la Recherche).

References

[1] Gornik E and Andronov A A (ed) 1991 *Opt. Quantum Electron.* **23** S111–360 (Special Issue on Far-infrared Semiconductor Lasers)
[2] Baraff G A 1962 *Phys. Rev.* **128** 2507
[3] Vosilius I I and Levinson I B 1966 *Sov. Phys.—JETP* **23** 1104
Vosilius I I and Levinson I B 1967 *Sov. Phys.—JETP* **25** 672
[4] Komiyama S 1982 *Adv. Phys.* **31** 255
[5] Starikov E, Shiktorov P, Gružinskis V, Reggiani L, Varani L and Vaissière J-C 2003 *J. Comput. Electron.* **2** 465
[6] Gružinskis V, Shiktorov P, Starikov E, Reggiani L, Varani L and Vaissière J C 2004 *Semicond. Sci. Technol.* **19** S173
[7] Gružinskis V, Starikov E and Shiktorov P 2005 *Acta Phys. Pol.* A **107** 163
[8] Gružinskis V, Starikov E and Shiktorov P 2007 *J. Comput. Electron.* **6** 11
[9] Matulionis A, Pozhela J and Reklaitis A 1975 *Phys. Status Solidi* a **31** 83
[10] Bareikis V, Galdikas A, Miliushyte R, Pozhela J and Viktoravichius V 1991 *J. Physique* **42** C7–215
[11] Pozhela Yu K, Starikov E V and Shiktorov P N 1992 *Semicond. Sci. Technol.* **7** B386
[12] Starikov E V and Shiktorov P N 1992 *Lietuvos Fizikos Rinkinis* **32** 471

[13] Shiktorov P N 1985 *Sov. Phys.—Collect.* **25** 59
[14] Kurosawa T and Kosano Y 1989 *Japan. J. Appl. Phys.* **58** 4104
[15] Ishida N and Kurosawa T 1995 *Japan. J. Appl. Phys.* **64** 2994
[16] Shiktorov P, Starikov E, Gružinskis V, Pérez S, González T, Reggiani L, Varani L and Vaissière J C 2003 *Phys. Rev.* B **67** 165201
[17] Bonch-Bruevich V L and El-Shamuby M A 1972 *Vestn. Moscow State Univ.* **13** 616
[18] Andronov A A and Kozlov V A 1973 *JETP Lett.* **17** 87
[19] Gulyaev Yu V and Chusov I I 1978 *Fiz. Tverd. Tela* **20** 2637
[20] Matulis A and Chenis A 1979 *Sov. Phys.—JETP* **50** 572
[21] Kustov V L, Ryzhii V I and Sigov Yu S 1980 *Sov. Phys.—JETP* **52** 1207
[22] Ryzhii V I, Bannov N A and Fedirko V A 1984 *Fiz. Tekh. Poluprovodn.* **18** 769
[23] Vorob'ev L E, Danilov S N, Tulupenko V N and Firsov D A 2001 *JETP Lett.* **73** 219
[24] Katayama Y and Komatsubara K F 1967 *Phys. Rev. Lett.* **19** 1421
[25] Hickmott T W, Solomon P M, Fang F F, Stern F, Fischer R and Morkoç H 1984 *Phys. Rev. Lett.* **52** 2053
[26] Lu P-F, Tsui D C and Cox H M 1985 *Phys. Rev. Lett.* **54** 1563
[27] Lu P-F, Tsui D C and Cox H M 1987 *Phys. Rev.* B **35** 9659
[28] Foutz B, O'Leary S, Shur M S and Eastman L F 1999 *J. Appl. Phys.* **85** 7727
[29] Brennan K and Hess K 1984 *Solid-State Electron.* **27** 347
[30] Price P J 1981 *Ann. Phys.* **133** 217
[31] Price P J 1984 *Phys. Rev.* B **30** 2234
[32] Price P J 1984 *Surf. Sci.* **143** 145
[33] Shiktorov P, Starikov E, Gružinskis V, Varani L, Palermo C, Millithaler J-F and Reggiani L 2007 *Phys. Rev.* B **76** 045333
[34] Starikov E, Shiktorov P, Gružinskis V, Reggiani L, Varani L, Vaissière J C and Zhao J H 2001 *J. Appl. Phys.* **89** 1161
[35] Starikov E, Shiktorov P, Gružinskis V, Reggiani L, Varani L, Vaissière J C and Zhao J H 2001 *IEEE Trans. Electron Devices* **48** 438
[36] Starikov E, Shiktorov P, Gružinskis V, Reggiani L, Varani L, Vaissière J C and Zhao J H 2001 *J. Phys.: Condens. Matter* **13** 7159
[37] Starikov E, Shiktorov P, Gružinskis V, Reggiani L, Varani L, Vaissière J C and Zhao J H 2002 *Mater. Sci. Forum* **384/385** 205
[38] Varani L, Vaissière J C, Starikov E, Shiktorov P, Gružinskis V, Reggiani L and Zhao J H 2002 *Phys. Status Solidi* a **190** 247
[39] Starikov E, Shiktorov P, Gružinskis V, Reggiani L, Varani L, Vaissière J C and Zhao J H 2002 *Physica* B **314** 171
[40] Starikov E, Shiktorov P, Gružinskis V, Dubinov A, Aleshkin V, Varani L, Palermo C and Reggiani L 2007 *J. Comput. Electron.* **6** 45
[41] Lu J T and Cao J C 2005 *Semicond. Sci. Technol.* **20** 829
[42] Korotyeyev V V, Kochelap V A, Kim K W and Woolard D L 2003 *Appl. Phys. Lett.* **82** 2643
[43] Kim K W, Korotyeyev V V, Kochelap V A, Klimov A A and Woolard D L 2004 *J. Appl. Phys.* **96** 6488
[44] Lu J T, Cao J C and Feng S L 2006 *Phys. Rev.* B **73** 195326
[45] Polyakov V M and Schiwierz F 2006 *J. Appl. Phys.* **100** 103704
[46] Starikov E, Shiktorov P, Gružinskis V, Reggiani L and Varani L 2007 *J. Nanoelectron. Optoelectron.* **2** 11
[47] Starikov E V and Shiktorov P N 1986 *Sov. Phys.—Semicond.* **20** 677
[48] Yariv A 1975 *Quantum Electronics* 2nd edn (New York: Wiley)
[49] Gružinskis V, Starikov E and Shiktorov P 2002 *Mater. Sci. Forum* **384/385** 213
[50] Starikov E, Gružinskis V and Shiktorov P 2002 *Phys. Status Solidi* a **190** 287
[51] Mitin V, Gruzhinskis V, Starikov E and Shiktorov P 1994 *J. Appl. Phys.* **75** 935
[52] Shiktorov P, Starikov E, Gružinskis V, Pérez S, González T, Reggiani L, Varani L and Vaissière J C 2006 *Semicond. Sci. Technol.* **21** 550
[53] Bannov N A, Ryzhii V I and Svyatchenko A A 1984 *Elektron. Tekh.-Ser. 3-Mikroelektron.* **107** 22
[54] Gružinskis V, Starikov E, Shiktorov P, Reggiani L, Saraniti M and Varani L 1993 *Simulation of Semiconductor Devices and Processes* vol 5 (Wien: Springer) p 333
[55] Ryzhii V, Satou A, Otsuji T and Shur M S 2008 *J. Appl. Phys.* **103** 014504